RSC Advances

PAPER

View Article Online
View Journal | View Issue

Cite this: *RSC Adv.*, 2018, **8**, 26888

Surface phosphation of 3D mesoporous $NiCo_2O_4$ nanowire arrays as bifunctional anodes for lithium and sodium ion batteries†

Wenda Qiu, *[ab] Hongbing Xiao,[a] Wenting He,[a] Juanhua Li,[a] An Luo,[a] Yu Li [a] and Yexiang Tong[b]

Received 14th June 2018
Accepted 24th July 2018

DOI: 10.1039/c8ra05128c

rsc.li/rsc-advances

A novel surface phosphate strategy was adopted to dramatically improve the charge transport, ion diffusion, electroactive sites, and cycle stability of mesoporous $NiCo_2O_4$ nanowire arrays (NWAs), drastically boosting their electrochemical properties. Consequently, the as-prepared phosphated $NiCo_2O_4$ NWA (P-$NiCo_2O_4$ NWA) electrode achieved excellent energy storage performance as a bifunctional anode material for both lithium ion batteries (LIBs) and sodium ion batteries (SIBs). When evaluated as an anode for LIBs, this P-$NiCo_2O_4$ NWA electrode showed a high reversible capacity up to 1156 mA h g^{-1} for 1500 cycles at 200 mA g^{-1} without appreciable capacity attenuation, while in SIBs, the electrode could also deliver an admirable initial capacity as high as 687 mA h g^{-1} and maintained 83.5% of this after 500 cycles at the same current density. Most important, when the current density increased from 100 to 1000 mA g^{-1}, the capacity retention was about 63% in LIBs and 54% in SIBs. This work may shed light on the engineering of efficient electrodes for multifunctional flexible energy storage device applications.

Introduction

Owing to the energy crisis and environmental pollution, there has been ever-increasing attention for exploring new energy storage technologies that are low-cost, environmentally friendly, safe, and efficient.[1–5] As a promising sustainable technology, Li ion batteries (LIBs) have been regarded as some of the most useful power source devices because of their high energy density, long cycle life, environmental benignity and other advantages, and they are widely used in electronics and electric vehicles.[6–9] While the LIBs are already sufficiently mature in technology, sodium ion batteries (SIBs) are getting more and more attention due to their own advantages, such as low cost, abundant resources and environmental friendliness.[10–13] Recently, a lot of new materials have been reported, such as fluoride-based ReO_3-type FeF_3,[14] layered transition metal oxides $Na_x[Fe_{1/2}Mn_{1/2}]O_2$,[15] P$_2$-$Na_xCoO_2$,[16] NASICON-type $Na_3V_2(PO_4)_3$,[17] cubic $Na_xMnFe(CN)_6$,[18] *etc.* In spite of the admirable developments of LIBs and SIBs,[5] it is urgent to make further breakthroughs on the electrode materials to satisfy the serious requirements for high energy density of SIBs and high power density of LIBs, particularly on anode materials.[19–21]

Transition metal oxides (TMOs) have been considered as an important class of functional materials for the development of next generation energy storage devices owing to their abundant oxidation states available for reversible redox reactions.[22–24] Among various TMOs, the spinel $NiCo_2O_4$ as a binary metal oxide is conceived as a very promising electrode material for energy storage since it owns high theoretical capacitance, cost effectiveness, abundant resources and eco-friendliness.[25–29] Unfortunately, the practical applications of $NiCo_2O_4$ were largely suffered from the slow faradaic redox kinetics, unsatisfied rate capability, and short cycle life.[30] There are two dominant techniques that are widely adopted to improve the electrochemical energy storage properties for LIBs and SIBs. While developing nanostructured electrode materials with large effective area is the first effective method. Nanoplatelets,[31] nanosheets,[27,32] nanowires,[25,33,34] nanoboxes,[35] microspheres,[28] have been studied, and showed better their electrochemical performance than their bulk counterparts. The second way is to combine electrode with highly conductive materials. For example, carbon materials, as superior electrical conductors, have been extensively applied to form composites with $NiCo_2O_4$ electrode.[22,25,36,37] Although the gratifying results have been

[a]*School of Eco-Environmental Technology, Guangdong Industry Polytechnic, 152 Xingang West Road, Guangzhou 510300, China. E-mail: Qiuwdgq@hotmail.com*

[b]*MOE of the Key Laboratory of Bioinorganic and Synthetic Chemistry, KLGHEI of Environment and Energy Chemistry, School of Chemistry, Sun Yat-Sen University, 135 Xingang West Road, Guangzhou 510275, China*

† Electronic supplementary information (ESI) available: SEM images, TEM images, XPS spectra, FTIR spectra, N_2 adsorption–desorption isotherm, CV and charge/discharge curves, linear sweep voltammetry curves and calculated linear resistivities of $NiCo_2O_4$ and P-$NiCo_2O_4$ NWAs. Cycling performance of P-$NiCo_2O_4$ NWAs with different phosphating temperature and different phosphating time. SEM image and P 2p core-level XPS spectrum of the P-$NiCo_2O_4$ NWAs after cycle. Long cycling test of the P-$NiCo_2O_4$ NWAs and carbon cloth for Li storage and Na storage. Comparison of lithium/sodium storage performance of different $NiCo_2O_4$ electrodes. See DOI: 10.1039/c8ra05128c

made, the cycle life and high rate performance are still unsatisfactory because of polarization, volume expansion/contraction, and insufficient active sites. Consequently, it is desirable to tailor nanoarchitecture design and engineer the surface of active materials, which could improve electrical/ion conductivity, increase activity sites, and maintain structural stability for long-time and high-rate cycling.

Herein, we report a novel approach to fabricate phosphated $NiCo_2O_4$ nanowire arrays (denoted as P-$NiCo_2O_4$ NWAs) on carbon cloth substrate. When evaluated as a bifunctional anode for LIBs and SIBs, surface phosphate play an important role in boosting the high-rate capacity tolerance and long-term stability for $NiCo_2O_4$ NWAs. There are many advantages in this well-designed electrode. First, the conductive carbon cloth with tight connection to the P-$NiCo_2O_4$ NWAs could be directly used as anode without any binder and conductive additives, which can ensure high mechanical stability and electric conductivity. Second, the unique 1D NWAs could provide rapid electron transport, efficient ion diffusion, and enhanced electrolyte penetration, which are beneficial to improve the capacity and rate capability for Li^+ and Na^+ storage. Third, surface phosphate could not only improve its conductivity, but also effectively tailor electrical, and provide more active sites for electrochemical reactions, leading to greatly improved capacitive performance. Furthermore, the mesoporous free-standing NWAs with a highly open structure could effectively buffer the volume variation during charge and discharge. Impressively, with the above merits, the P-$NiCo_2O_4$ NWAs exhibits exceptional high-rate capability and long-term stability as an anode material for LIBs and SIBs.

Experimental

Preparation of P-$NiCo_2O_4$ NWAs

All of the chemical reagents used in this experimental are analytical grade without any further processing. Typically, $CoCl_2 \cdot 6H_2O$ (2.38 g), $NiCl_2 \cdot 6H_2O$ (1.19 g), and urea (0.9 g) were dissolved in 75 mL deionized water at room temperature under vigorous magnetic stirring. After being magnetically stirred for 1 h, the solution together with a piece of clean carbon cloth (3 cm × 4 cm) were transferred into a 50 mL Teflon-lined stainless steel autoclave. The autoclave was kept at 120 °C in the oven 6 h, and then cooled down to room temperature. The $NiCo_2O_4$ NWAs were corrected from the autoclave, and washed with deionized water and ethanol for six times and calcined at 300 °C under air atmosphere for 60 min. According to the previous literature,[38] the P-$NiCo_2O_4$ NWAs were obtained by further annealed at 250 °C for 60 min in Ar atmosphere with the presence of $NaH_2PO_2 \cdot H_2O$ (500 mg).

Materials characterization

The morphology, structure and chemical composition of the electrode materials were investigated by scanning electron microscopy (SEM; JSM-6330F), transmission electron microscopy (TEM, FEI Tecnai G2 F30), XPS (ESCALab 250, Thermo VG), Fourier transform infrared spectroscopy (FTIR, Nicolet/Nexus 670), Raman spectroscopy (Renishaw inVia), X-ray diffractometry (D8 ADVANCE), and Brunauer–Emmet–Teller (BET, Micromeritics ASAP 2010 analyzer).

Battery assembly and electrochemical measurements

All of the electrochemical measurements were performed on the CR2032-type coin cells, which were assembled in an argon-filled glovebox (Mikrouna, Co., Ltd.). The as-fabricated carbon cloth supported P-$NiCo_2O_4$ NWAs electrode was cut into circular pieces with diameter 12 mm, which directly used as anode for LIBs and SIBs without any binder and conductive additive. The mass loading of the P-$NiCo_2O_4$ NWAs was calculated about 2.5 mg cm^{-2}. For assembling LIBs, a lithium foil and Cellgard 2400 film were used as the counter electrode amd separator, respectively. A solution of 1 M $LiPF_6$ in ethylene carbonate (EC)/diethyl carbonate (DEC) (1 : 1 in volume) was used as electrolyte. Similarly, the fabrication of SIBs was under the same conditions. A sodium foil, Cellgard 2400 film and a solution containing 1 M $NaClO_4$ in a mixture of EC/DEC/DEC (1 : 1 : 0.05 in volume) were used as the counter electrode separator, and electrolyte, respectively. The charge/discharge was performed by Neware battery testing system in a voltage window from 0.01 V to 3.0 V at room temperature. Cyclic Voltammogram (CV) measurements were collected on Autolab with a scanning rate of 0.2 mV s^{-1}. The electrochemical impedance spectroscopy (EIS) were also measured in a frequency range of 0.01–100 kHz.

Results and discussion

Our design of bifunctional additive-free anode began with the vertical growth of $NiCo_2O_4$ NWAs precursors on carbon cloth through a facile hydrothermal method. By subsequent calcining in air at 300 °C for 60 min, the precursors were converted into $NiCo_2O_4$ NWAs. To obtain P-$NiCo_2O_4$ NWAs, the $NiCo_2O_4$ NWAs were further phosphidation with PH_3 in Ar atmosphere, as illustrated in Fig. 1a. Low magnification image (Fig. 1b) reveals that the entire surface of carbon cloth was covered with densely ordered $NiCo_2O_4$ NWAs with a length of about 1–3 μm. The comparison between $NiCo_2O_4$ NWAs and P-$NiCo_2O_4$ NWAs indicates that the morphological of $NiCo_2O_4$ NWAs are well preserved after phosphidation (Fig. 1c and S1†). The typical transmission electron microscopy (TEM) image further reveals the diameter of the P-$NiCo_2O_4$ NWAs ranged from 120 to 160 nm with a length of several micrometer (Fig. 1d), which is well consistent with SEM observation. Moreover, we can see that porous are scattered around the whole surface of the P-$NiCo_2O_4$ NWAs. As displayed in Fig. S2,† this mesoporous structure is also demonstrated by the Barrett–Joyner–Halenda pore size distribution curves, revealing NWAs being reconstructed with smaller particles and pores. Specifically, the high surface area together with porous networks in our well-designed 3D architecture provide more active sites, rapid ion diffusion and exceptional electrolyte accessibility. Additionally, the corresponding selected area electron diffraction (SAED) pattern in the inset of Fig. 1d betokens the polycrystalline nature of the P-$NiCo_2O_4$ NWAs. Furthermore, the lattice fringes shown in the

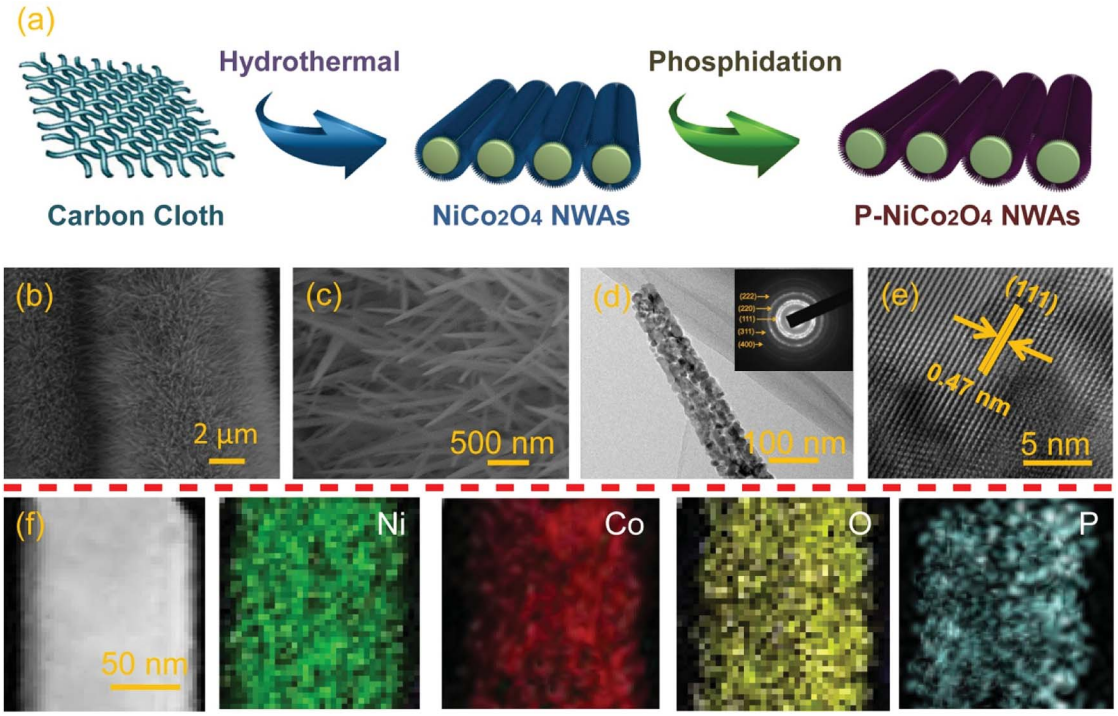

Fig. 1 (a) Schematic illustration of the synthesis process; (b) low and high (c) magnification SEM images; (d) low and (e) high magnification TEM images; and (f) STEM images for P-$NiCo_2O_4$ NWAs. The inset in (d) is the corresponding SAED pattern.

inset of Fig. 1e is measured to be 0.47 nm, corresponding to (111) crystal planes of the spinel $NiCo_2O_4$ phase. Fig. S3† is the typical TEM image of the pristine $NiCo_2O_4$ NWAs, showing both samples have similar mesoporous structure, and surface phosphation results in a decreased crystallinity for P-$NiCo_2O_4$ NWAs. Additionally, the energy dispersive X-ray spectroscopy under scanning transmission electron microscopy (STEM) observation clearly demonstrates that Ni, Co, O, and P element distributions are uniform throughout the whole NWAs (Fig. 1f), manifesting completely phosphate on the surface.

To determine the possible phase and composition change of the products during phosphidation treatment, X-ray diffraction (XRD), Raman and X-ray photoelectron spectroscopy (XPS) analyses were conducted. Typical XRD patterns of the pristine $NiCo_2O_4$ NWAs and P-$NiCo_2O_4$ NWAs samples are collected in Fig. 2a. Comparing with standard peaks, the original $NiCo_2O_4$ NWAs could be well assigned to the spinel $NiCo_2O_4$ phase (JCPDS card no. 20-0781), signifying the obtained $NiCo_2O_4$ NWAs sample is high purity. After surface phosphation, the P-$NiCo_2O_4$ NWAs still contain typical diffraction peaks of spinel $NiCo_2O_4$ phase, but the relative intensity of diffraction peaks are decreases obviously as compared to the pristine $NiCo_2O_4$ NWAs, which is in good agreement with the HRTEM measurements. The above XRD results implying no phase transformation occurred during the surface phosphation and the decreased crystallinity for P-$NiCo_2O_4$ NWAs. As observed in Fig. 2b, the Raman spectra of both samples reveal four characteristic peaks at 190, 478, 525, and 671 cm^{-1}, corresponding to the F_{2g}, E_g, F_{2g}, and A_{1g} models of $NiCo_2O_4$, respectively.[39] No signal ascribed to phosphate or hydroxides can be observed in Raman spectra, which prove again that no phase transition after surface phosphation. Furthermore, X-ray photoelectron spectroscopy (XPS) was also adopted to make a thorough inquiry into surface phosphation. Broad scan of the P-$NiCo_2O_4$ NWAs implies the existence of Ni, Co, O, and P, as well as C from the reference, and there are no other impurities being detected (Fig. S4a†), which again demonstrate that the phosphate ions have been successfully introduced to the surface of $NiCo_2O_4$ NWAs. In the high resolution Ni 2p spectrum (Fig. 2c), the fitting peaks at 854 and 871.2 are indexed to Ni^{2+}, while those at 856.1 and 873.5 belong to Ni^{3+}. In comparison with the pristine $NiCo_2O_4$ NWAs, the peaks of the P-$NiCo_2O_4$ NWA shifted towards more negative values, revealing the oxygen vacancies are created in P-$NiCo_2O_4$ NWA during surface phosphidation treatment.[40,41] Similar evidence is also verified by the high resolution Co 2p XPS spectra in Fig. 2d. Moreover, the O 1s core-level XPS spectra shows one strong peak centered at 530 eV (Fig. 2e), which are generally put down to typical metal–oxygen bonds.[42] The shoulder peak located at 531.5 eV for the pristine $NiCo_2O_4$ NWAs is related to the presence of hydroxyl groups (–OH) on the $NiCo_2O_4$ NWAs.[43] In contrast, the shoulder peak for the P-$NiCo_2O_4$ NWAs is well fitted into two components locating at 531.7 and 532.6 eV, which correspond to the oxygen species of $(H_2PO_4)^-$ and $(PO_3)^-$, respectively.[38,44] Evidently, –OH on the $NiCo_2O_4$ NWAs surface have been replaced by the phosphate ion species during the surface phosphidation process. Furthermore, the P 2p core-level XPS spectrum (Fig. 2f) and Fourier transform infrared spectroscopy (Fig. S4b†) of the P-$NiCo_2O_4$

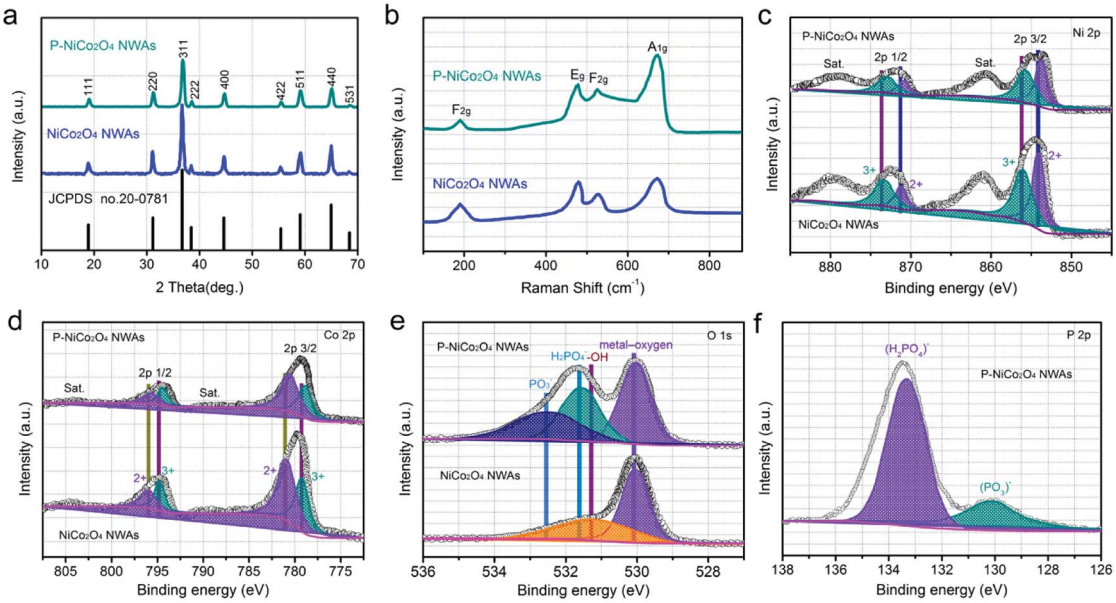

Fig. 2 (a) XRD spectra and (b) Raman spectra of $NiCo_2O_4$ NWAs and P-$NiCo_2O_4$ NWAs. High-resolution XPS spectra of (c) Ni 2p, (d) Co 2p, (e) O 1s and (f) P 2p for P-$NiCo_2O_4$ NWAs. All of the above characterization tests were scratched down from the carbon cloth.

NWAs further prove that the $(H_2PO_4)^-$ and $(PO_3)^-$ are existence on the surface of $NiCo_2O_4$ NWAs. As expected for surface phosphidation, the above results unambiguously reveal that the phosphate ions have been successfully introduced to the surface of $NiCo_2O_4$ NWAs.

Lithium storage performance

To probe the redox reaction during the charging and discharging process of LIBs, cyclic voltammograms (CV) curves of the pristine $NiCo_2O_4$ NWAs and P-$NiCo_2O_4$ NWAs (Fig. 3a, S5a and b†) were carried out between 0.01 and 3.0 V *vs.* Li/Li^+ at a sweep rate of 0.2 mV s^{-1}. Three redox current peaks could be distinctly distinguishable from the both CVs, indicating the electrochemical reaction pathway of the two electrodes are very similar.[37,45] As clearly shown in the pristine $NiCo_2O_4$ NWAs curves, the cathodic located at about 0.91 V could relate to the reduction of Ni^{2+} and Co^{3+} to metallic Ni and Co. By contrast, there are two anodic peaks are situated at 1.61 and 2.26 V, which maybe accredited to the oxidation of Ni to NiO_x, and Co to CoO_x,

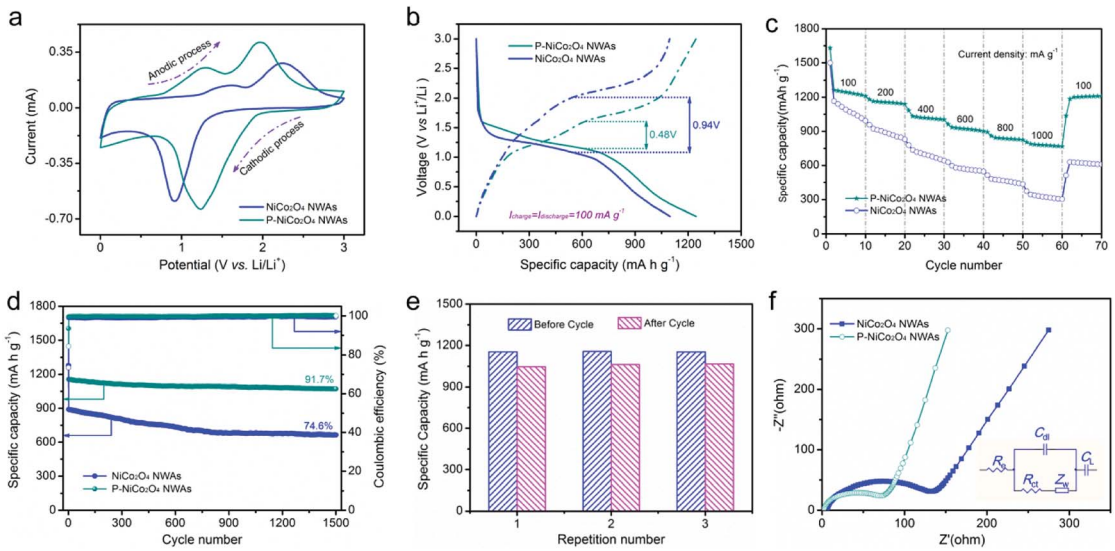

Fig. 3 (a) CV curves (0.2 mV s^{-1}) and (b) galvanostatic charge/discharge curves (100 mA g^{-1}) after five cycles activation, (c) rate capability, (d) cycling performance, and (f) Nyquist plots of the $NiCo_2O_4$ NWAs and P-$NiCo_2O_4$ NWAs electrodes. (e) Duplicate test of the P-$NiCo_2O_4$ NWAs electrodes.

respectively.[28] The overall lithiation and delithiation processes occurring in the $NiCo_2O_4$ NWAs electrode could be reformulated with more detail as follows:

$$NiCo_2O_4 + 8Li^+ + 8e^- \leftrightarrow Ni + 2Co + 4Li_2O \quad (1)$$

$$Ni + Li_2O \leftrightarrow NiO + 2Li^+ + 2e^- \quad (2)$$

$$Co + Li_2O \leftrightarrow CoO + 2Li^+ + 2e^- \quad (3)$$

$$Co + \frac{1}{3}Li_2O \leftrightarrow \frac{1}{3}Co_3O_4 + \frac{1}{3}Li^+ + \frac{1}{3}e^- \quad (4)$$

Comparing with the original $NiCo_2O_4$ NWAs electrode, there are one cathodic peak (1.23 V) and two anodic peak (1.29 and 1.98 V) in the P-$NiCo_2O_4$ NWAs electrode. It is obvious that there is a difference in redox peaks between the two samples, which maybe attributed to the smaller polarization and enhance surface electrochemical activity in P-$NiCo_2O_4$ NWAs electrode after surface phosphation.[1,46] Besides, for the purpose of a better determination polarization, the overpotential is derived from the difference between charge and discharge potential ($\Delta V/2$) at the half reversible capacity ($Q/2$).[1,46–48] As observed in Fig. 3b, the overpotential of P-$NiCo_2O_4$ NWAs is only 0.48 V, which is much smaller than the value of pristine $NiCo_2O_4$ NWAs electrode (0.94 V), demonstrating a better electrical and ionic conductivity.

A high rate capability of the electrode is important to achieve high power densities. Fig. 3c, S5c and d† display the high-rate performance of the both electrodes. Apparently, the P-$NiCo_2O_4$ NWAs electrode deliveries discharge capacities of 1245, 1156, 1019, 924, 838, and 779 mA h g^{-1} at the current of 100, 200, 400, 600, 800, 1000 mA g^{-1}, respectively, which are significantly larger than the corresponding values of pristine $NiCo_2O_4$ NWAs electrode. It is encouraging that the P-$NiCo_2O_4$ NWAs electrode could still maintain the high capacity (1207 mA h g^{-1}) at 100 mA g^{-1}, demonstrating its superior rate reversibility. Such very high specific capacity and rate performance could be compared with or even larger than the values of other $NiCo_2O_4$-based anode materials (Table S1†), such as rGO/$NiCo_2O_4$ nanocomposite,[22] $NiCo_2O_4$/carbon textiles,[25] $NiCo_2O_4$ hollow spheres,[28] flower-type $NiCo_2O_4$,[36] $NiCo_2O_4$ nanoribbons,[49] and UNF@$NiCo_2O_4$.[50] Indeed, the P-$NiCo_2O_4$ NWAs electrode could retain an ultrahigh capacity retention of 62.6% when the discharge current changed from 100 to 1000 mA g^{-1}, and this high rate capability is considerably superior to the untreated $NiCo_2O_4$ NWAs electrode (30%) and other reported anodes.[22,25,28,51–54]

Electrochemical stability is a critical issue for P-$NiCo_2O_4$ NWAs electrode that severely impedes their practical application. We examined the cycling stability of the untreated $NiCo_2O_4$ NWAs and P-$NiCo_2O_4$ NWAs electrodes with a current density of 200 mA g^{-1} (Fig. 3d). Evidently, the pristine $NiCo_2O_4$ NWAs electrode undergo an apparent capacity fading during the cycling durability test, and only 664 mA h g^{-1} is maintained after 1500th cycles. In contrast, the P-$NiCo_2O_4$ NWAs electrode has an outstanding cycling stability. Even after 1500 cycles, a high reversible specific capacity over 1071 mA h g^{-1} is achieved at a current density of 200 mA g^{-1}, which is equal to 91.7% of the 2nd discharge capacity. Furthermore, the Coulombic efficiency of the P-$NiCo_2O_4$ NWAs electrode is more than 99% except for the 1st cycle, prefiguring an admirable reversibility and stability during the charge–discharge process. More importantly, its excellent electrochemical stability is highly reproducible since high capacity retention (ranging from 90.6% to 92.5%) is obtained for the three P-$NiCo_2O_4$ NWAs electrodes (Fig. 3e). Additionally, the effect of phosphating temperature and phosphating time on the electrochemical performance of the P-$NiCo_2O_4$ NWAs were also studied, and found that 250 °C phosphating temperature and 60 min phosphating time exhibits the best performance (Fig. S6†). The cycling stability achieved in the P-$NiCo_2O_4$ NWAs electrode is better than most of the reported $NiCo_2O_4$ materials, including flower-like $NiCo_2O_4$,[55] $NiCo_2O_4$ nanosheets,[56] $NiCo_2O_4$/C nanorods,[57] $NiCo_2O_4$ hollow spheres,[28] and UNF@$NiCo_2O_4$ (ref. 50) (see detailed comparison in Table S1†). Moreover, the SEM and XPS collected from P-$NiCo_2O_4$ NWAs after 1500 cycles further confirm that the surface phosphation and the unique porous nanowire arrays structure can substantially improve the lithium storage performance of $NiCo_2O_4$ NWAs electrode (Fig. S7†).

Meanwhile, electrochemical impedance spectroscopy (EIS) is employed to examine the effect of surface phosphation on the kinetics of charge and ionic transport in the treated and untreated $NiCo_2O_4$ NWAs electrodes (Fig. 3f). Notably, the charge transfer resistance (R_{ct}) of $NiCo_2O_4$ NWAs electrode is measured to be 126.6 Ω, and yet the corresponding R_{ct} of P-$NiCo_2O_4$ NWAs electrode is only 68 Ω, meaning that its superior conductivity as a result of the surface phosphation. Additionally, the slope of the straight line of the P-$NiCo_2O_4$ NWAs electrode is substantially steeper than that of the untreated $NiCo_2O_4$ NWAs electrode, showing that the P-$NiCo_2O_4$ NWAs electrode has a much faster ion diffusion rate (Fig. S8†). The above EIS results for the two samples are in good agreement with the overpotential analyses. Benefiting from the surface phosphation, there are sufficient electroactive sites, less polarization, fast charge transport, and rapid ion diffusion in the P-$NiCo_2O_4$ NWAs electrode, and consequently greatly improve the high-rate capability and long-term stability.

Sodium Storage Performance

It is well known that a good electrode material for NIBs has its own unique structure, such as layered structure, open framework, and a well-tailored architecture, which could effectively accommodate larger volume changes comparing with LIBs.[1,58–60] It was motivated by such reasons, we anticipate that surface phosphation could modify the electrochemical activity of $NiCo_2O_4$ NWAs and promote its sodium storage performance. Given the advantages of surface phosphation above mention, we further make a discussion about sodium storage performance merely based on the P-$NiCo_2O_4$ NWAs electrode, and the corresponding data are showed in Fig. 4.

The CV curves in Fig. 4a exhibit two cathodic peaks centered at about 0.86 and 0.26 V, corresponding to the reduction of

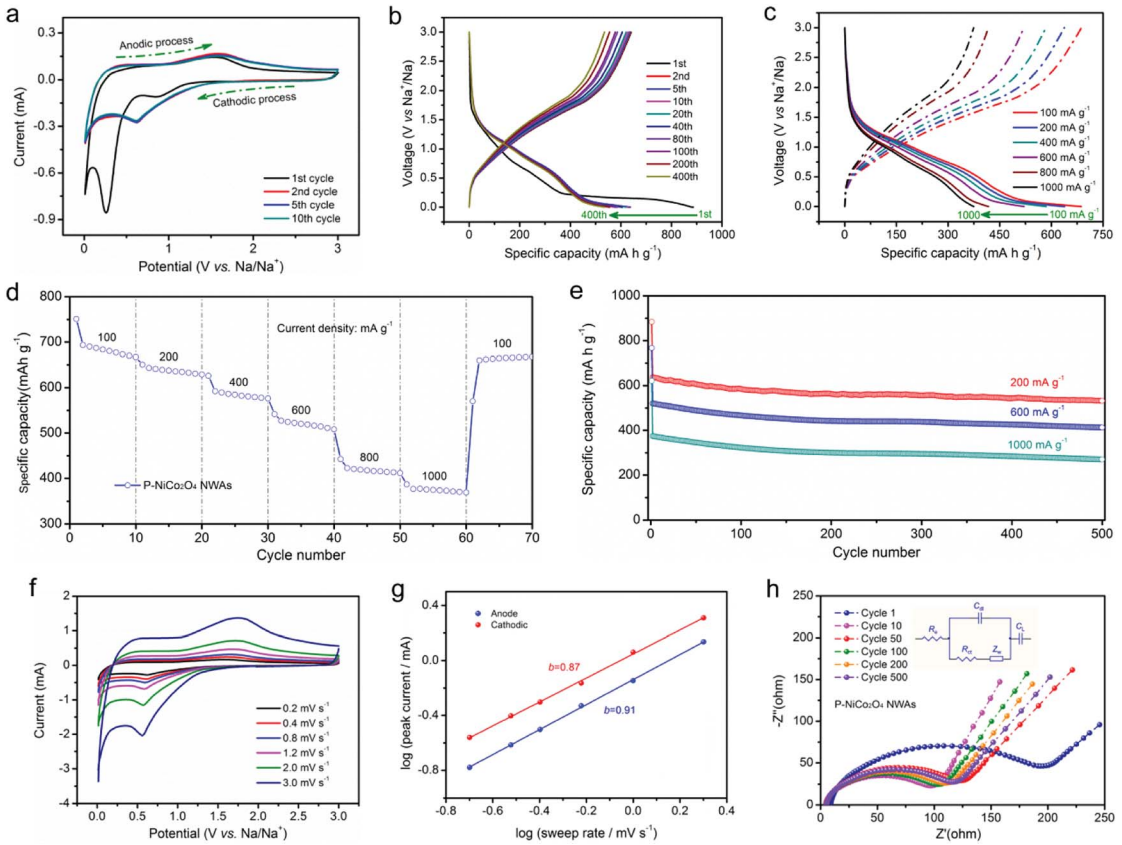

Fig. 4 Sodium Storage Performance of P-$NiCo_2O_4$ NWAs electrode: (a) CV curves at 0.2 mV s^{-1}, (b) charge–discharge curves at 200 mA g^{-1}, (c) charge–discharge curves under different current density, (d) rate performance, (e) cycling performance, (f) CV curves with different scan rates, (g) plots of log(scan rate) again log(peak current), which calculated from CV curves in (f), and (h) Nyquist plots.

$NiCo_2O_4$ and the formation of Na_2O ($NiCo_2O_4 + 8Na^+ + 8e^- \rightarrow Ni + 2Co + 4Na_2O$).[35,53] It is clear that the reduction peak of the sample was shifted to approximately 0.62 V from the second cycle, which could be attributed to the irreversible reaction resulting from the decomposition of electrolyte and the formation of SEI film.[14] Meanwhile, there are two anodic peaks located at around 0.56 and 1.60 V, which could be relate to the oxidation of Co to Co^{3+} and Ni to Ni^{2+}.[53,61]

It is suggested that the sodium storage behavior could be investigated using "conversion" reaction by means of discharging to 0.005 V.[62] As depicted in Fig. 4b, except for a lower voltage and capacity, the charge–discharge curves of SIBs are similar to that of LIBs. This is because the sodium ion has a larger radius than lithium ion, and leading to a slower thermodynamics and kinetics for sodium storage.[63] The first discharge curve displays a sloping curve with a flat wide plateau at 0.25 V, which could be due to the phase decompose of the spinel structure.[35] The little difference between the cycles in charge/discharge process proves that the sodiation reaction is highly reversible. Moreover, even at high current densities, the P-$NiCo_2O_4$ NWAs electrode still remained a high capacity and superior capacity retention (Fig. 4c and d).

Specifically, when the current increase from 100 to 200, 400, 600, 800, and 1000 mA g^{-1}, the P-$NiCo_2O_4$ NWAs electrode achieves a specific capacities as high as 687, 638, 585, 521, 417, and 375 mA h g^{-1}, respectively. And even more exciting when the current returned to 100 mA g^{-1}, the specific capacity still can return to 665 mA h g^{-1}, which adequately prove that P-$NiCo_2O_4$ NWAs can withstand high rate cycling. Such excellent rate performance is in sharp contrast to those reported $NiCo_2O_4$ and other metal oxides electrode, for example, mesoporous $NiCo_2O_4$ nanosheets,[32] three-dimensional $NiCo_2O_4$ nanowire arrays,[53] hollow urchin-like $NiCo_2O_4$ microspheres,[64] $NiCo_2O_4$ nanowire array,[65] and hollow $NiCo_2O_4$ nanoboxes[35] (listed in Table S2†). Furthermore, the P-$NiCo_2O_4$ NWAs electrode also represents a remarkable cycle stability for sodium storage (Fig. 4e). At 200 mA g^{-1}, a specific capacity of 532 mA h g^{-1} is obtained after 500 cycles, and what is more, even the current density raise to 600 and 1000 mA g^{-1}, 413 and 270 mA h g^{-1} are still remained after 500 cycles, respectively. Additionally, to probe the sodium storage kinetics of P-$NiCo_2O_4$ NWAs electrode, the CV measurements at varied sweep rates were conducted. As shown in Fig. 4f, the CV curves with various scan rates are very similar, and even if the scan rate increased to 15 times, there are no significant changes in the position and shape of the current peaks, demonstrating rapid Na^+ insertion/extraction kinetics in the P-$NiCo_2O_4$ NWAs electrode. To confirm this point again, the peak current is logarithmically plotted *versus* scan rates (Fig. 4g), which usually appears in a linear relation. Generally, the current (i) and sweep rates (v)

have a relationship on $i = av^b$, and comply with the power law (a and b are adjustable parameters).[6,66] The value of b, calculated from the slope of the $\log(v) - \log(i)$ plots, can be used to distinguish the type of the charge storage mechanism. Specifically, a b-value of 1.0 involves a typical capacitive (or surface) process, whereas 0.5 signifies a diffusion-controlled process.[6,13,67] The calculated b-values for cathodic peaks is 0.87, while the corresponding value for the anodic peaks is 0.91, illustrating a pseudocapacitive behavior for Na storage in the P-$NiCo_2O_4$ NWAs. Besides, to further elucidate the kinetics of ionic and charge transport in the P-$NiCo_2O_4$ NWAs electrode, we survey the EIS during long-term cycle. As shown in Fig. 4h, the Nyquist plots of the P-$NiCo_2O_4$ NWAs electrode can be well fitted by the equivalent circuit. It is worth noting that the R_{ct} of the electrode drop rapidly during the first 50 cycles, while raise marginally in subsequent cycles, which is ascribed to the slow kinetic activation process of the electrode. The subsequent mild R_{ct} increase because of the tiny polarization, revealing an excellent long-term durability for the electrode and great promise as an anode for SIBs.

Here it is appropriate to premeditate the surface phosphation mechanism and briefly discuss the key factors for superior electrochemical performance of this elaborate electrode. Generally, the $Na_2PO_2 \cdot H_2O$ will decompose and form PH_3 gas at temperature greater than 150 °C according to the eqn (5). In the presence of PH_3 gas and H_2O gas, the $NiCo_2O_4$ was reduced to $NiCo_2O_{4-x}$ and covered with H_3PO_4 at same time, as shown in eqn (6). It is worth noting that the presence of the H_2O gas played a vital role in obtaining P-$NiCo_2O_4$ instead of nickel cobalt phosphides. It is well known that materials with a lower solubility product constant (K_{sp}) value are more favorable in reactions than those with higher K_{sp} values.[68,69] According to previous reports,[68,70] the magnitude of K_{sp} for nickle cobalt hydroxide is about 10^{-15}, and the corresponding value for nickle cobalt phosphate is approximately 10^{-31}. Accordingly, as soon as the $H_2PO_4^-$ ions are absorbed at the surface, ion exchanges between $H_2PO_4^-$ and OH^- occur on the surface of $NiCo_2O_{4-x}$.

$$2Na_2PO_2 \cdot H_2O \rightarrow PH_3\,(g)\uparrow + Na_2HPO_4\,(s) + 2H_2O\,(g)\uparrow \quad (5)$$

$$NiCo_2O_4 + \frac{x}{4}PH_3 \rightarrow NiCo_2O_{4-x} + \frac{x}{4}H_3PO_4 \quad (6)$$

As schematically shown in Fig. 5, the outstanding electrochemical performance in LIBs and SIBs of this well-designed electrode could be ascribed to the following advantages: (1) The free-standing 1D nanowires are beneficial to improve the conductivity and maintain structural stability. (2) The surface phosphation could provide more active sites, and dramatically increase capacitive performance. (3) The porous mesoporous structure in 1D nanowires not only furnish more surface area for surface redox reaction, but also afford suitable channels for lithium and sodium intercalation/deintercalation. (4) The carbon cloth serve as flexible and high conductivity current collector, which can fast charge transport, rapid ion diffusion and accommodate mechanical strains. It is worth mentioning

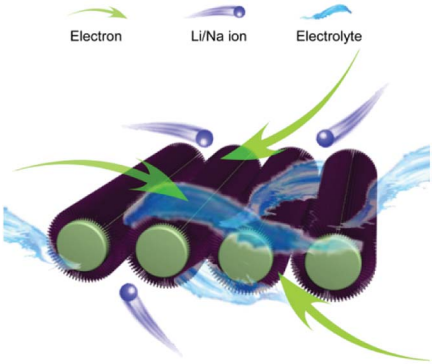

Fig. 5 Schematic illustration of the P-$NiCo_2O_4$ NWAs electrode with smooth Li/Na ion and electron transfer channels.

that the carbon cloth provides a nontrivial contribution to the capacity (Fig. S9†). The surface phosphation offers the merit of rich active sites, higher specific surface area, improving the conductivity and kinetics, thereby leading to exceptional rate capability and good long-term stability in both LIBs and SIBs.

Conclusions

In summary, the surface phosphated $NiCo_2O_4$ NWAs have been developed and attested as advanced bifunctional anode for lithium and sodium ion battery. Benefiting from the flexible 3D carbon cloth support, sufficient active sites, fast charge transport, rapid ion diffusion, and excellent structural stability, the as-prepared electrode showed remarkable capacitive performance and long cycle life for LIBs and SIBs. When the P-$NiCo_2O_4$ NWAs as anode for LIBs, the electrode yields a high capacity outstrip 1156 mA h g^{-1} with more than 91.7% retention after 1500 cycles at 200 mA g^{-1}. Furthermore, an admirable capacity of 687 mA h g^{-1} together with an impressive rate tolerance and superior capacitance retention (72% after 500 cycles at 1000 mA g^{-1}) can be achieved as SIBs electrode. The present work may shed light on the improvement of electrochemical performances for other metal oxides, and provides new opportunities for high-performance flexible electrochemical storage and conversion devices.

Conflicts of interest

There are no conflicts to declare.

Acknowledgements

This work was supported by the Science and Technology Planning Project of Guangzhou (201804010196), Guangdong Province Higher Vocational Colleges & Schools Pearl River Scholar Funded Scheme (2015), Natural Science Foundation of Guangdong Province (2016A030313761), Research project of Guangdong Industry Polytechnic (KJFH2018-001), Science and Technology Planning Project of Foshan (2017AB003922), Foshan research center for special functional building materials and its green preparation technology (2017-203), Opening

Foundation of MOE Key Laboratory of Bioinorganic and Synthetic Chemistry Sun Yat-Sen University (2016), The innovative project course of Guangdong Industry Polytechnic (2017–2018 2nd semester), the Pearl River Scholar Foundation of Guangdong Industry Polytechnic (RC2015-001), and Education Commission of Guangdong Province (2017GkQNCX002, 2017GKCXTD001).

Notes and references

1 D. Chao, C. Zhu, X. Xia, J. Liu, X. Zhang, J. Wang, P. Liang, J. Lin, H. Zhang and Z. X. Shen, *Nano Lett.*, 2014, **15**, 565.
2 X. Zhang, G. Zhu, M. Wang, J. Li, T. Lu and L. Pan, *Carbon*, 2017, **116**, 686.
3 X. Wang, L. Fan, D. Gong, J. Zhu, Q. Zhang and B. Lu, *Adv. Funct. Mater.*, 2016, **26**, 1104.
4 C. Wu, P. Kopold, P. A. van Aken, J. Maier and Y. Yu, *Adv. Mater.*, 2017, **29**, 1604015.
5 Y. Xu, M. Zhou and Y. Lei, *Adv. Energy Mater.*, 2016, **6**, 1502514.
6 L. Shen, S. Chen, J. Maier and Y. Yu, *Adv. Mater.*, 2017, **29**, 1701571.
7 S. Wang, B. Y. Guan, L. Yu and X. W. D. Lou, *Adv. Mater.*, 2017, **29**, 1702724.
8 J. Zhang, L. Yu and X. W. D. Lou, *Nano Res.*, 2017, **10**, 4298.
9 L. Yu, J. F. Yang and X. W. D. Lou, *Angew. Chem., Int. Ed.*, 2016, **55**, 13422.
10 Z. Liu, T. Lu, T. Song, X.-Y. Yu, X. D. Lou and U. Paik, *Energy Environ. Sci.*, 2017, **10**, 1576.
11 Y. Fang, X. Y. Yu and X. W. D. Lou, *Angew. Chem., Int. Ed.*, 2017, **56**, 5801.
12 Z. Liu, X.-Y. Yu, X. W. D. Lou and U. Paik, *Energy Environ. Sci.*, 2016, **9**, 2314.
13 F. Niu, J. Yang, N. Wang, D. Zhang, W. Fan, J. Yang and Y. Qian, *Adv. Funct. Mater.*, 2017, **27**, 1700522.
14 C. Li, C. Yin, L. Gu, R. E. Dinnebier, X. Mu, P. A. van Aken and J. Maier, *J. Am. Chem. Soc.*, 2013, **135**, 11425.
15 N. Yabuuchi, M. Kajiyama, J. Iwatate, H. Nishikawa, S. Hitomi, R. Okuyama, R. Usui, Y. Yamada and S. Komaba, *Nat. Mater.*, 2012, **11**, 512.
16 R. Berthelot, D. Carlier and C. Delmas, *Nat. Mater.*, 2011, **10**, 74.
17 S. Li, Y. Dong, L. Xu, X. Xu, L. He and L. Mai, *Adv. Mater.*, 2014, **26**, 3545.
18 L. Wang, Y. Lu, J. Liu, M. Xu, J. Cheng, D. Zhang and J. B. Goodenough, *Angew. Chem., Int. Ed.*, 2013, **52**, 1964.
19 Y. Xu, Y. Zhu, Y. Liu and C. Wang, *Adv. Energy Mater.*, 2013, **3**, 128.
20 X. Wang, L. Fan, D. Gong, J. Zhu, Q. Zhang and B. Lu, *Adv. Funct. Mater.*, 2016, **26**, 1104.
21 B. Zhang, J. Huang and J. K. Kim, *Adv. Funct. Mater.*, 2015, **25**, 5222.
22 L. Zhang, H. B. Wu and X. W. D. Lou, *Adv. Energy Mater.*, 2014, **4**, 1300958.
23 P. Poizot, S. Laruelle, S. Grugeon, L. Dupont and J. Tarascon, *Nature*, 2000, **407**, 496.
24 L. Zhang, H. B. Wu and X. W. D. Lou, *Adv. Energy Mater.*, 2014, **4**, 1300958.
25 L. Shen, Q. Che, H. Li and X. Zhang, *Adv. Funct. Mater.*, 2014, **24**, 2630.
26 C. Yuan, J. Li, L. Hou, X. Zhang, L. Shen and X. W. D. Lou, *Adv. Funct. Mater.*, 2012, **22**, 4592.
27 G. Zhang and X. W. D. Lou, *Adv. Mater.*, 2013, **25**, 976.
28 L. Shen, L. Yu, X. Y. Yu, X. Zhang and X. W. D. Lou, *Angew. Chem., Int. Ed.*, 2015, **54**, 1868.
29 G. Zhang and X. W. D. Lou, *Adv. Mater.*, 2013, **25**, 975.
30 C. Guan, X. Liu, W. Ren, X. Li, C. Cheng and J. Wang, *Adv. Energy Mater.*, 2017, **7**, 1602391.
31 B. Cui, H. Lin, J. B. Li, X. Li, J. Yang and J. Tao, *Adv. Funct. Mater.*, 2008, **18**, 1440.
32 K. Zhou, Z. Hong, C. Xie, H. Dai and Z. Huang, *J. Alloys Compd.*, 2015, **651**, 24.
33 L. Mai, X. Tian, X. Xu, L. Chang and L. Xu, *Chem. Rev.*, 2014, **114**, 11828.
34 H. Sun, Y. Zhang, J. Zhang, X. Sun and H. Peng, *Nat. Rev. Mater.*, 2017, **2**, 17023.
35 J. Chen, Q. Ru, Y. Mo, S. Hu and X. Hou, *Phys. Chem. Chem. Phys.*, 2016, **18**, 18949.
36 C. Zhang and J. S. Yu, *Chem.–Eur. J.*, 2016, **22**, 4422.
37 Y. Chen, M. Zhuo, J. Deng, Z. Xu, Q. Li and T. Wang, *J. Mater. Chem. A*, 2014, **2**, 4449.
38 T. Zhai, L. Wan, S. Sun, Q. Chen, J. Sun, Q. Xia and H. Xia, *Adv. Mater.*, 2016, **29**, 1604167.
39 D. Zhang, H. Yan, Y. Lu, K. Qiu, C. Wang, Y. Zhang, X. Liu, J. Luo and Y. Luo, *Dalton Trans.*, 2014, **43**, 15887.
40 Y. Zeng, Y. Han, Y. Zhao, Y. Zeng, M. Yu, Y. Liu, H. Tang, Y. Tong and X. Lu, *Adv. Energy Mater.*, 2015, **5**, 1402176.
41 X. Lu, G. Wang, T. Zhai, M. Yu, J. Gan, Y. Tong and Y. Li, *Nano Lett.*, 2012, **12**, 1690.
42 E. Umeshbabu, G. Rajeshkhanna, P. Justin and G. R. Rao, *RSC Adv.*, 2015, **5**, 66657.
43 L. Huang, D. Chen, Y. Ding, S. Feng, Z. L. Wang and M. Liu, *Nano Lett.*, 2013, **13**, 3135.
44 K. Ghosh, E. R. M. Balog, P. Sista, D. J. Williams, D. Kelly, J. S. Martinez and R. C. Rocha, *APL Mater.*, 2014, **2**, 021101.
45 Y. Chen, J. Zhu, B. Qu, B. Lu and Z. Xu, *Nano Energy*, 2014, **3**, 88.
46 M.-S. Balogun, Y. Luo, F. Lyu, F. Wang, H. Yang, H. Li, C. Liang, M. Huang, Y. Huang and Y. Tong, *ACS Appl. Mater. Interfaces*, 2016, **8**, 9733.
47 C. Niu, J. Meng, C. Han, K. Zhao, M. Yan and L. Mai, *Nano Lett.*, 2014, **14**, 2873.
48 L. Hu, F. La Mantia, H. Wu, X. Xie, J. McDonough, M. Pasta and Y. Cui, *Adv. Energy Mater.*, 2011, **1**, 1012.
49 B. Li, J. Feng, Y. Qian and S. Xiong, *J. Mater. Chem. A*, 2015, **3**, 10336.
50 J. Pu, Z. Liu, Z. Ma, J. Wang, L. Zhang, S. Chang, W. Wu, Z. Shen and H. Zhang, *J. Mater. Chem. A*, 2016, **4**, 17394.
51 P. Liang, H. Zhang, F. Ling, Y. Bai and W. Yu, *ACS Appl. Mater. Interfaces*, 2016, **8**, 4745.
52 L. Liu, H. Zhang, J. Yang, Y. Mu and Y. Wang, *J. Mater. Chem. A*, 2015, **3**, 22393–22403.

53 Y. Mo, Q. Ru, J. Chen, X. Song, L. Guo, S. Hu and S. Peng, *J. Mater. Chem. A*, 2015, **3**, 19765.
54 X. Zhou, G. Chen, J. Tang, Y. Ren and J. Yang, *J. Power Sources*, 2015, **299**, 97.
55 L. Li, Y. Cheah, Y. Ko, P. Teh, G. Wee, C. Wong, S. Peng and M. Srinivasan, *J. Mater. Chem.*, 2013, **1**, 10935.
56 A. K. Mondal, D. Su, S. Chen, K. Kretschmer, X. Xie, H. J. Ahn and G. Wang, *ChemPhysChem*, 2015, **16**, 169.
57 L. Peng, H. Zhang, Y. Bai, J. Yang and Y. Wang, *J. Mater. Chem. A*, 2015, **3**, 22094.
58 S. Tepavcevic, H. Xiong, V. R. Stamenkovic, X. Zuo, M. Balasubramanian, V. B. Prakapenka, C. S. Johnson and T. Rajh, *ACS Nano*, 2011, **6**, 530.
59 D. Su and G. Wang, *ACS Nano*, 2013, **7**, 11218.
60 Z. Chen, V. Augustyn, X. Jia, Q. Xiao, B. Dunn and Y. Lu, *ACS Nano*, 2012, **6**, 4319.
61 A. Thissen, D. Ensling, F. J. Fernández Madrigal, W. Jaegermann, R. Alcántara, P. Lavela and J. L. Tirado, *J. Mater. Chem.*, 2005, **17**, 5202.
62 S. Hariharan, K. Saravanan, V. Ramar and P. Balaya, *Phys. Chem. Chem. Phys.*, 2013, **15**, 2945.
63 C. Zhu, X. Mu, P. A. van Aken, Y. Yu and J. Maier, *Angew. Chem., Int. Ed.*, 2014, **53**, 2152.
64 X. Zhang, Y. Zhao, C. Wang, X. Li, J. Liu, G. Yue and Z. Zhou, *J. Mater. Sci.*, 2016, **51**, 9296.
65 J.-W. Lee, H.-S. Shin, C.-W. Lee and K.-N. Jung, *Nanoscale Res. Lett.*, 2016, **11**, 1–9.
66 H. Lindström, S. Södergren, A. Solbrand, H. Rensmo, J. Hjelm, A. Hagfeldt and S.-E. Lindquist, *J. Phys. Chem. B*, 1997, **101**, 7717.
67 H. Liang, J. Ni and L. Li, *Nano Energy*, 2017, **33**, 213.
68 Y. Zhao, Z. Chen, D.-B. Xiong, Y. Qiao, Y. Tang and F. Gao, *Sci. Rep.*, 2016, **6**, 17613.
69 X. Xia, C. Zhu, J. Luo, Z. Zeng, C. Guan, C. F. Ng, H. Zhang and H. J. Fan, *Small*, 2014, **10**, 766.
70 I. Shakir, M. Sarfraz, U. A. Rana, M. Nadeem and M. A. Al-Shaikh, *RSC Adv.*, 2013, **3**, 21386.